Chemical mechanical polishing of powder bed fusion – laser beam processed 316 L stainless steel

Journal of Materials Processing Tech. 345 (2025) 119055

Contents lists available at ScienceDirect

Journal of Materials Processing Tech.

journal homepage: www.elsevier.com/locate/jmatprotec

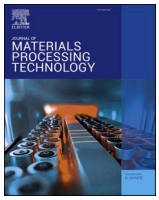

Research article

Chemical mechanical polishing of powder bed fusion – laser beam processed 316 L stainless steel

Rasmus Gunnerek [a,*], Gowtham Soundarapandiyan [a], Tatiana Mishurova [b], Jakob Schröder [b], Giovanni Bruno [b], Joshua Boykin [c], Agustin Diaz [c], Uta Klement [a], Eduard Hryha [a]

[a] Industrial and Materials Sciences, Chalmers University of Technology, Gothenburg, SE 412 96, Sweden
[b] Bundesanstalt für Materialforschung und -prüfung (BAM), Unter den Elchen 87, Berlin 12205, Germany
[c] REM Surface Engineering, 2107 Longwood Drive, Brenham, TX, USA

ARTICLE INFO

Keywords:
Additive manufacturing
Chemical mechanical polishing
As-built microstructure
Surface roughness
Surface finishing
Material removal
Residual stress

ABSTRACT

Additive manufacturing via powder bed fusion – laser beam (PBF-LB) enables the fabrication of complex geometries but suffers from inherently rough surfaces and surface tensile residual stresses, both of which can compromise structural integrity, particularly under fatigue loading. To address these limitations, this study investigates chemical mechanical polishing (CMP) as a surface finishing method for improving surface quality and modifying the residual stress state in PBF-LB 316 L stainless steel. The work uniquely examines how scan rotation (0° vs. 67° rotation) and contour parameters influence CMP effectiveness in material removal, surface smoothing, and subsurface stress redistribution. With a targeted material removal of 110 μm, CMP reduced surface roughness (*Sa*) by up to 94 %, achieving values as low as 0.7 μm. Microstructural analysis revealed no grain refinement but identified a thin, plastically deformed surface layer. This plastic deformation resulted in the transformation of tensile surface stresses (340 MPa) into beneficial compressive stresses (−400 MPa), as confirmed by synchrotron X-ray diffraction, which also showed a shift toward isotropic strain distribution. Further, these findings demonstrate that the initial scan strategy influences CMP performance and that CMP can enhance both surface integrity and mechanical reliability without altering the underlying microstructure. This study advances the understanding of how process induced microstructure and surface features affect CMP outcomes, enabling more informed design of post-processing strategies for improved surface integrity and mechanical performance in additively manufactured metals.

1. Introduction

Powder bed fusion – laser beam (PBF-LB) enables production of complex geometries, which are difficult or not possible to produce by conventional manufacturing processes. While the PBF-LB process has gained greater acceptance with the enhanced densification of several materials, with static properties comparable to those produced by conventional means, the complicated surface topography and high residual stresses of PBF-LB materials remain a great challenge. The surfaces of PBF-LB components are typically associated with average surface roughness (*Ra*) values between 3 and 50 μm. Rough surfaces with deep valleys can act as critical sites characterized by high-stress concentration and localized strain accumulation that evidently cause crack initiations and premature failure in fatigue loading [1,2]. This roughness is a consequence of different aspects related to the process, such as the powder feedstock, process parameters, and component design [3].

As-built surfaces are distinguished by a primary roughness attributed to melt pool solidification. The melt pools are the building blocks of the process, and their connection to each other can yield significant differences in roughness. Typically, the melt pool morphology provides a certain waviness to the final surface. Another unique feature of PBF-LB surfaces is the secondary roughness characterized by partially or fully melted powder particles that adhere to the surface. The roughness can, to some extent, be reduced by optimizing parameters, such as applying a contour parameter. After the bulk scan is performed, the contour scans the outer surface of the part, which, if optimized, smoothens the melt pool boundaries, reduces powder adhesion, and limits dross formation [4,5]. Although roughness reductions can be achieved through proper

* Corresponding author.
E-mail address: rasmus.gunnerek@chalmers.se (R. Gunnerek).

https://doi.org/10.1016/j.jmatprotec.2025.119055
Received 30 March 2025; Received in revised form 1 September 2025; Accepted 4 September 2025
Available online 6 September 2025

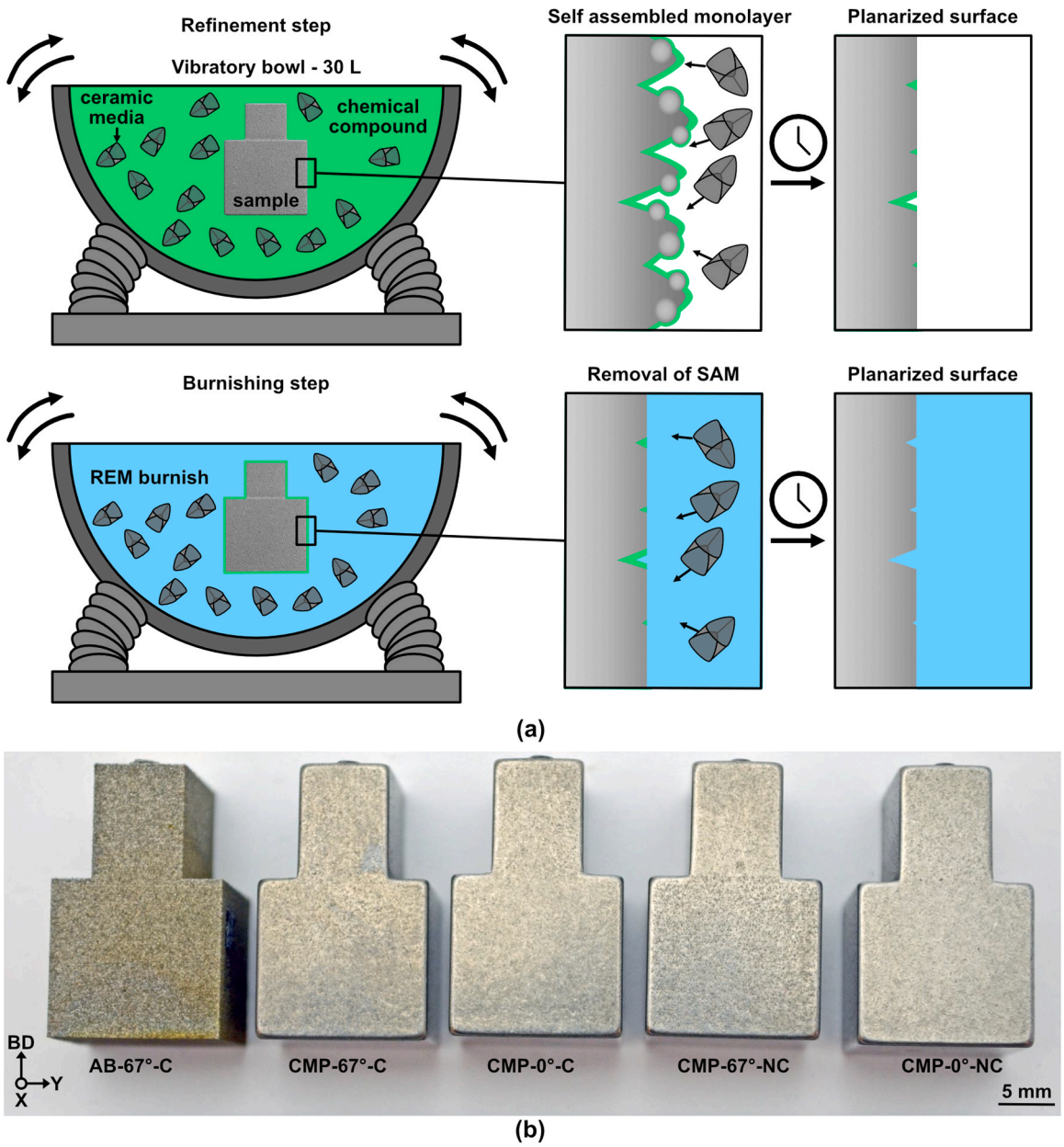

Fig. 1. Overview of the CMP process and its effects. (a) Schematic of the two-step CMP process. (b) Image of specimens in as-built and CMP-processed states. CMP treatment results in smoother, shinier surfaces with rounded edges, attributed to increased localized media contact during vibratory motion.

optimizing of parameters, for more demanding applications and fatigue loading, the surfaces need further improvement.

Beyond surface irregularities, the cyclic rapid melting and solidification inherent in PBF-LB generate large thermal gradients, accumulating residual stresses. These stresses can result in part deformation or cracking [6]. Generally, as the material solidifies, a contraction takes place where tensile stresses are generated at the surface and compressive stresses in the bulk. Thus, typical residual stress profiles in PBF-LB components, where tensile stresses are prevalent at the surface, are transitioning to compressive stresses in the interior [7]. These surface tensile stresses can negatively impact fatigue life by intensifying crack initiation at surface features [8,9].

Various surface treatments have been explored to reduce roughness and residual stresses. Conventional approaches like machining effectively reduce roughness and enhance fatigue life of PBF-LB produced materials by eliminating surface and subsurface defects [2,10]. However, the complex designs of PBF-LB components, such as small features or internal cooling channels, are difficult or impossible to access, requiring new innovative surface finishing strategies [11,12].

Researchers have investigated a variety of surface treatment techniques to satisfy the needs of PBF-LB surfaces. These can be grouped by their mechanism and effects. A rough distinction can be made between treatments using mechanical/abrasive, chemical/ electrochemical, or hybrid methods to alter the surface topography of PBF-LB surfaces [13]. Mechanical treatments studied on PBF-LB surfaces, such as shot peening, offer a combination of lowered roughness and beneficial compressive stresses that improve mechanical performance [14,15]. However, as the process relies on the physical impact of process media, shot peening heavily deforms the surface microstructure and struggles with internal geometries and fine geometrical features [16]. Other studied surface treatments, such as chemical polishing, provide homogeneous material removal even for internal features because material removal is driven by selectively dissolving surface features by chemical reaction. This has been proven efficient at reducing the roughness of 316 L stainless steel as

Table 1
Chemical composition of AISI 316 L stainless steel powder in wt%.

Chemical composition	C	Ni	Cr	Mo	Mn	Si	O	Fe
wt%	0.028	12.6	16.9	2.5	1.5	0.7	0.056	Balance

low as Ra = 0.4 μm [17]. However, the process also has its limitations, such as uneven material removal due to microstructural differences and high chemical consumption with possible environmental impacts [18].

The CMP process, also known as chemically accelerated vibratory finishing (CAVF), is another cost-efficient hybrid alternative that combines mechanical and chemical-driven material removal. The CMP or CAVF process is based on accelerating the surface material removal (SMR) via a self-limiting chemical reaction while the components are in a vibratory bowl. Usually, the CMP process does not require abrasive media, and a gentler media (ceramics, porcelains, or plastics) is employed to decrease the media attrition rate (media last longer), rounding off edges, and smaller features. During CMP processing, a material specific compound activates the surface by forming a self-assembling monolayer (SAM), which is easy to remove by any rubbing action, accelerating the removal of surface peaks by the non-abrasive media [19,20].

A handful of studies have investigated the CMP process on PBF-LB materials such as titanium [21,22], nickel-based superalloys [20,21], stainless steel [23] and copper [19]. The process has been shown to enhance the surface finish with Ra below 0.1 μm without changing the microstructure and improving the corrosion properties of 316 L processed via CMP [23]. However, a dedicated analysis of the surface microstructure and how the process influences residual stress distribution is missing. One of the great benefits of PBF-LB is that the microstructure can be tailored locally through changes in e.g. process parameters or scan strategy. Therefore, it is important to see how different post-processing operations, such as CMP, impacts the printed microstructures. As the surface roughness improvement evolves through SMR, a greater understanding of the depth of material that should be removed must be considered. It is well established that different scan strategies and process parameters can yield significant differences in surface roughness, microstructure, and subsurface defects.

Despite the demonstrated potential of CMP to improve surface finish and corrosion resistance in PBF-LB metals, its mechanistic interactions with as-built surface features, specifically those governed by scan strategy, remain poorly understood. Prior research has largely focused on surface roughness improvements, with limited attention to how initial microstructure and topography affect material removal behaviour, surface deformation, or residual stress redistribution during CMP. To fill these gaps, this study investigates the influence of scan rotation (0° and 67°) and contour parameters on CMP outcomes in PBF-LB/316 L stainless steel. Through quantitative surface characterization, microstructural analysis, and synchrotron X-ray diffraction, the work examines how CMP modifies roughness, induces plastic deformation, and transforms surface tensile stresses into isotropic compressive stress. By establishing these process–structure–property relationships, this work provides a scientific basis for tailoring CMP post-processing to enhance surface integrity and fatigue resistance in additively manufactured components.

2. Materials and methodology

2.1. Powder feedstock and sample manufacturing

Two sets of specimens with a shape consisting of a 15 × 15 × 15 mm^3 cube in the bottom and a top 8 × 15 × 10 mm^3 (Fig. 1b) were manufactured of gas atomized 316 L stainless steel powder (20–53 μm) from Höganäs AB using an EOS M290 system (EOS GmbH). The chemical composition of the powder is presented in Table 1. A layer thickness of 40 μm and a standard parameter set (316 L_040_FlexM291_1.00) were employed. Two scan rotation strategies were implemented to generate distinct microstructures. The first set utilized a 67° rotation, representing the state-of-the-art approach. The second set employed a 0° rotation, designed to create a more anisotropic microstructure [24], as used in previous work [25]. For each scan rotation, specimens were fabricated with and without contour parameters, referred to as C = contour and NC = no contour, respectively, in subsequent figures and discussion.

2.2. Chemical mechanical polishing

The PBF-LB 316 L specimens underwent surface finishing via CMP, provided by REM Surface Engineering (Brenham, Texas). The mechanism and workflow of the CMP process are illustrated in Fig. 1a, with the resulting surface conditions shown in Fig. 1b. Treatment was performed in a 30 L vibratory bowl filled with non-abrasive, high-density ceramic media (straight-cut triangles, 3 mm × 5 mm), operated at a frequency of 54 Hz, a 3 mm amplitude, and a lead angle of 80°.

During the refinement step, a proprietary REM 316 L chemical compound was dosed at 1litre per hour (L/h) in a flow-through configuration for 6 h. This formulation reacts with the stainless-steel surface to form a thin conversion layer, SAM or oxide that weakens atomic bonding at surface irregularities [23,26]. The layer is subsequently removed through mechanical rubbing by the ceramic media, enabling preferential smoothing of surface peaks. Approximately 110 μm of material was removed per surface during this stage. Following refinement, a burnishing step was conducted in the same vibratory setup. The chemical input was switched to a diluted REM burnishing compound (1:100 in water), dosed at 5 L/h for 1 h. This step deactivates and removes the conversion layer while further enhancing optical smoothness and surface uniformity.

2.3. Surface topography characterization

The surface topography measurements of the as-built and CMP processed surfaces were performed in a SensoFar Neox S optical profilometer with a Nikon objective at 20 x magnification utilizing confocal fusion on stitched areas of 3.2 × 2.4 mm of the BD-Y plane parallel to the build direction. Surface plots and roughness measurements were processed and extracted in Mountains Map 10.1 [27]. Specific surface texture parameters were chosen and compared (S_a, S_{10z}) following the ISO 25178–2 standard [28]. The surface topography of samples in as-built condition and after CMP treatment were studied in SEM.

2.4. Microstructural characterization

All microstructural investigations were performed on the XY-plane, perpendicular to the build direction, to capture the surface/subsurface features and to estimate the amount of material removal. Samples were sectioned using a high-speed saw with a diamond blade and ground using SiC abrasive paper (P180 grit - P1200 grit). Polishing was performed using 9, 3, and 1 μm diamond suspension. The samples were electrochemically etched in 10 % oxalic acid at 3 V to reveal features such as melt pools, grain boundaries, and cells. The part surface and microstructure were characterized before and after CMP using light optical microscopy (LOM) with a Zeiss Axioscope 7 and scanning electron microscopy (SEM) with a Zeiss Gemini 450 field emission microscope. All samples selected for electron backscattered diffraction (EBSD) mapping were further polished using OP-S colloidal silica suspension to remove any deformation remaining from the previous polishing steps.

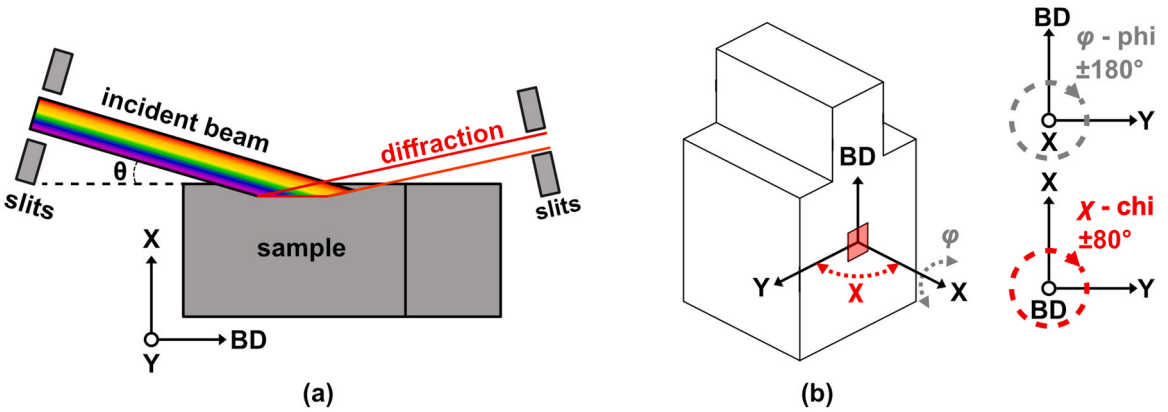

Fig. 2. The experimental diffraction setup. (a) relationship between incident white beam and diffraction (b) coordinate system for different acquisition angles φ and χ.

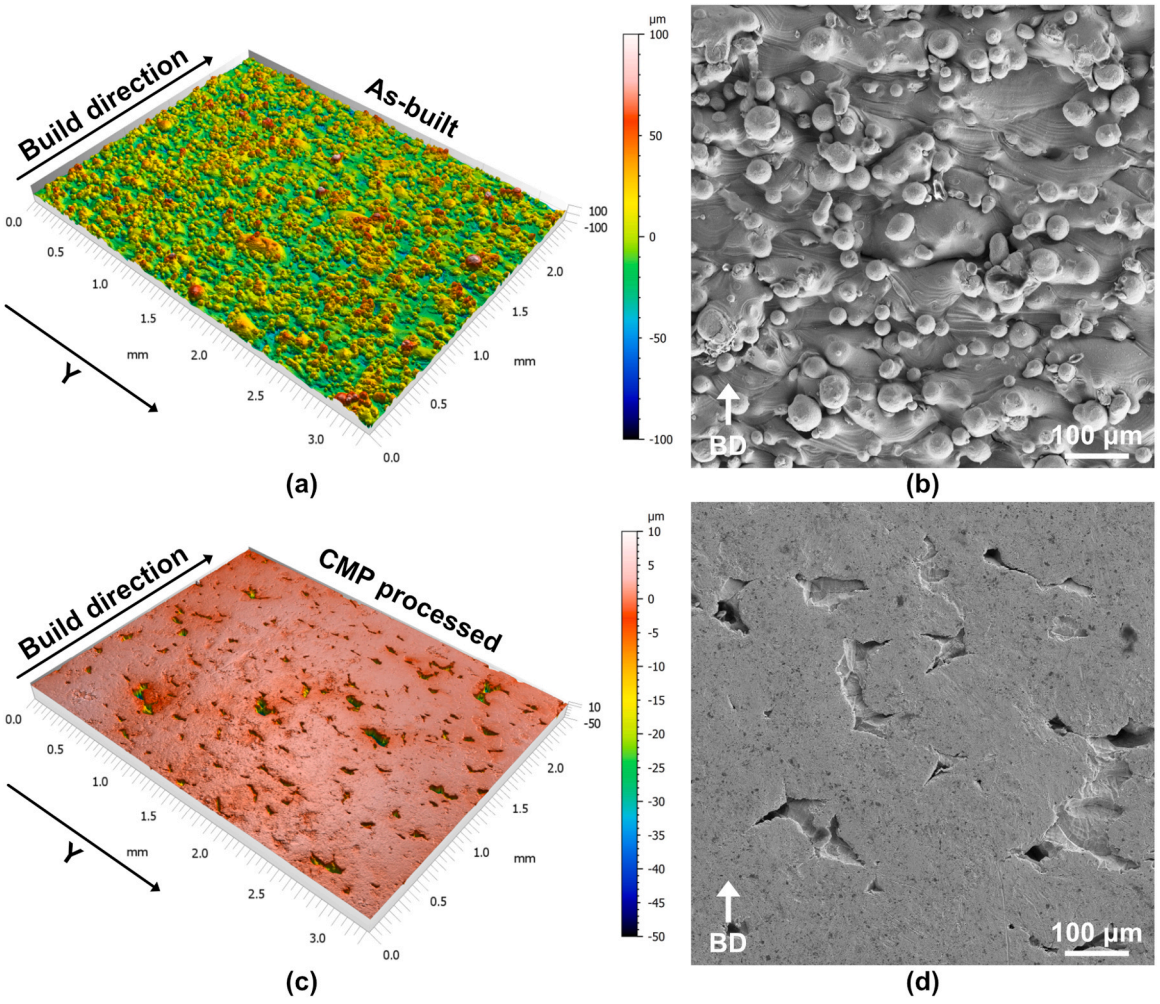

Fig. 3. Surface topography for 67° scan rotation with contour illustrated by surface plots. (a) as-built condition and (c) after CMP treatment. SEM images of the same surfaces (b) as-built condition and (d) after CMP treatment.

2.5. EBSD and KAM maps

Large area mapping of the as-built and CMP processed microstructure was acquired using the Zeiss Gemini 450 using electron backscatter diffraction (EBSD) at an acceleration voltage of 20 kV with 1.5 μm step size. Higher magnification EBSD acquisitions for Kernel Average Misorientation (KAM) maps used a smaller step size of 0.2 μm with a maximum misorientation angle of 2° to remove the impact of grain boundaries. After the acquisition, all EBSD data was processed in AztecCrystal3.3.

2.6. Energy dispersive synchrotron X-ray diffraction

The energy dispersive - synchrotron X-ray diffraction (ED-SXRD)

Table 2
Areal roughness measurements of as-built and CMP processed conditions.

Condition	*Sa* (μm)	*Sa* reduction (%)	*S10z* (μm)	*S10z* reduction (%)
AB−67°-C	15.9	-	156.2	-
AB−0°-C	10.9	-	105.0	-
AB−67°-NC	19.2	-	189.7	-
AB−0°-NC	12.5	-	121.4	-
CMP−67°-C	1.5	90.6	49.6	68.2
CMP−0°-C	1.1	90.0	50.5	51.9
CMP−67°-NC	4.4	77.1	98.8	47.9
CMP−0°-NC	0.7	94.4	28.2	76.8

measurements were performed at the white beam engineering materials science beamline P61A at the Deutsches-Elektronen-Synchrotron (DESY) in Hamburg, Germany [29]. In essence, an energy dispersive detector detects the energy (E^{hkl}) of the X-rays diffracted by the sample at a fixed diffraction angle θ. In such case, Bragg's law can be rewritten in terms of photon energy with h being the plank constant, c the speed of light, and d^{hkl} the lattice spacing [30]:

$$d^{hkl} = \frac{h \cdot c}{2\sin\theta} \bullet \quad \frac{1}{E^{hkl}} \tag{1}$$

Due to the wide energy spectrum of the white synchrotron beam, the retrieved information arises from different depths, providing depth resolution. The originating depth from which 63 % of the total diffracted intensity originates can be calculated for each lattice plane by considering the acquisition setup [31]. A simplified illustration of the basic instrument principle in reflection geometry is shown in Fig. 2. Prior to the measurements, calibration was performed using the diffraction angle of $2\theta = 7.10823°$ and NIST silicon powder. The specimens, mounted in an Eulerian cradle, were scanned in χ-mode using the energy-dispersive detector in the vertical diffraction plane ($\chi = \psi$ for the detector in the vertical diffraction plane). Therefore, the calculation of the information depth τ is given by Eq. 2, with μ denoting the energy dependent mass absorption coefficient [31]:

$$\tau(hkl) = \frac{\sin\theta}{2\mu}\cos\psi \tag{2}$$

To reduce the background signal on the detector, anti-scattering slits were used. The specimens were measured in the BD-Y plane (see Fig. 2). Beam conditions were optimized to avoid saturation of the detector at different tilt angles: for $\chi = 0–36°$ 50 mm graphite in the incoming beam with 6 s acquisition time, for $\chi = 40–56°$ 40 mm graphite in the incoming beam with 7 s acquisition time, and for $\chi = 60–80°$ 30 mm graphite in the incoming beam with 8 s acquisition time. In addition, the incoming beam was narrowed by the vertical and horizontal slits to a 0.5×0.5 mm^2 cross section. In the diffracted beam, the slits narrowed the beam to 50×50 μm^2. The full φ range of 360° was mapped with a step size of 15°, whereas χ angles were measured with 4° step size, resulting in a total number of 504 acquisitions per sample. The schematic in Fig. 2b highlights the relationship between the sample coordinates and φ and χ acquisition angles.

Peak fitting was performed in the open-source software P61A:Viewer developed at the P61A beamline, using a pseudo-Voigt function [32]. Peaks under 100 counts were excluded from the subsequent residual stress analysis.

2.7. Residual stress analysis

For each reflection, the residual stress was determined using the least-squares method as proposed by Ortner [33]. In this context, Hooke's law can be written in the special form of Dölle & Hauk (Eq. 3). Such equation relates the strain in the laboratory system $\langle \varepsilon^{L}_{\varphi\psi} \rangle$ to the stress $\langle \sigma^{S}_{ij} \rangle$ in the sample coordinate system. The so-called X-ray elastic stress factors $F_{33ij}(\varphi, \psi, hkl)$ contain information on the coordinate transformation and the elastic stiffness of the material [34]. The stress factor entities were determined from the single-crystal elastic constants of 316 L ($c_{11} = 206$ GPa, $c_{12} = 133$ GPa, $c_{44} = 119$ GPa) [35] using the Kröner model in ISODEC [36]. For the strain calculation, the average of all measured lattice distances was used as the stress-free reference. Using such a stress-free reference, the overdetermined linear equation system

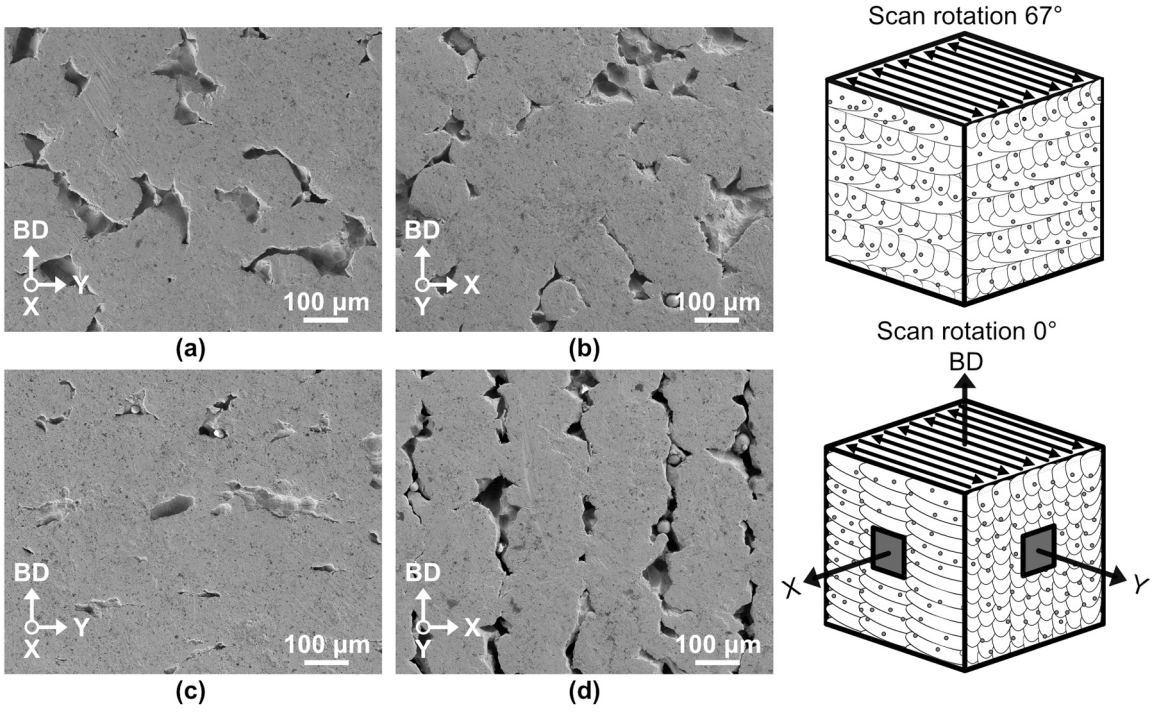

Fig. 4. SEM images of different surfaces and cross sections processed by CMP. (a) BD-Y and (b) BD-X for 67°-NC scan rotation (c) and (d) 0°-NC scan rotation for BD-Y and BD-X cross-sections respectively, with simplified schematics for each scan rotation presented to the right of the micrographs.

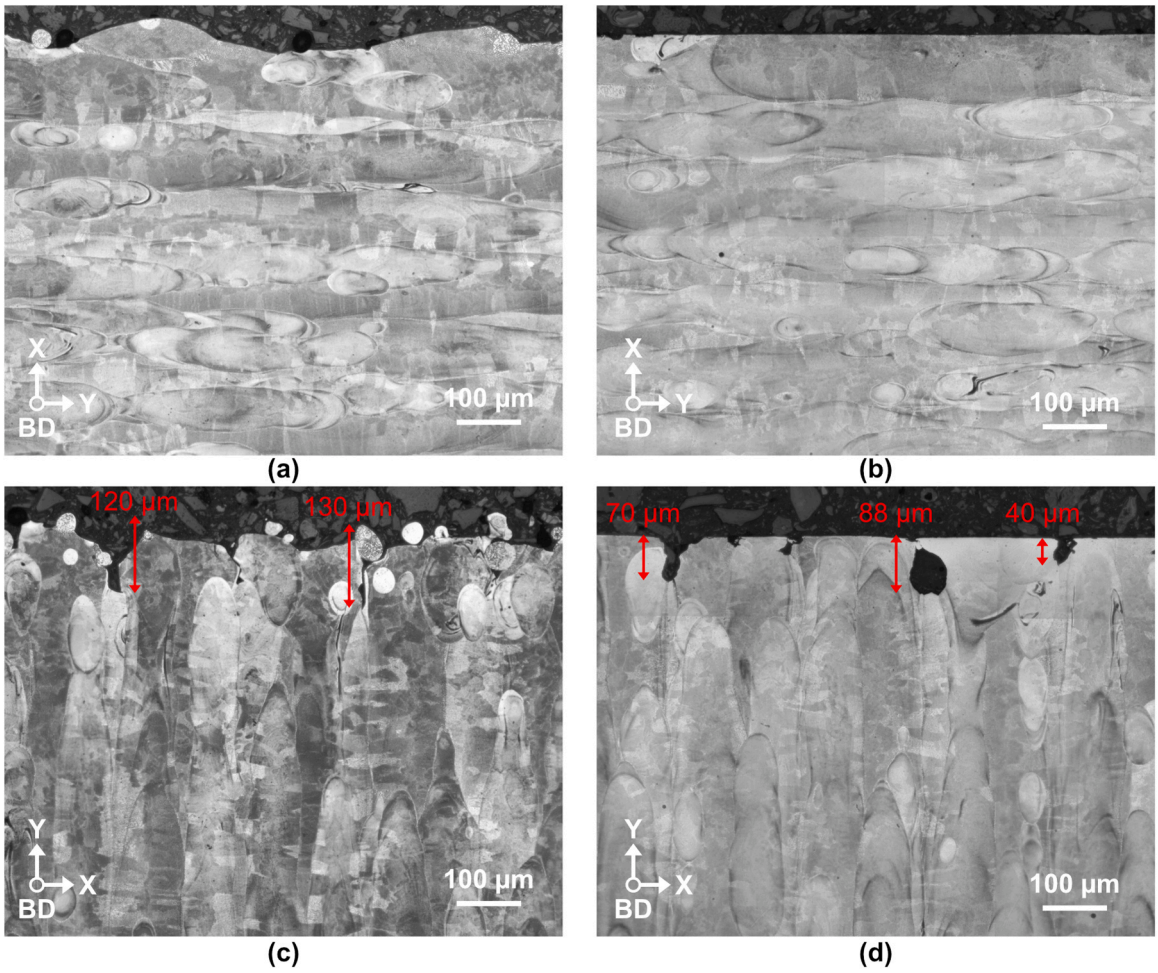

Fig. 5. Optical micrographs of etched XY-cross sections. (a) and (c) as-built condition and b) and d) after CMP processing for 0° scan rotation without contour.

was solved using in-house python code. Since the choice of such a stress-free reference is arbitrary, the results are expressed as deviatoric stresses, so the dependence on the stress-free reference is removed.

$$\left\langle \varepsilon_{33}{}^{L} \right\rangle = \left\langle \varepsilon^{L}_{\varphi\psi} \right\rangle = \frac{d^{hkl}(\varphi,\psi,311) - d_0^{hkl}(\varphi,\psi,311)}{d_0^{hkl}(\varphi,\psi,311)}$$

$$= \sum_{ij=1}^{3} F_{33ij}(\varphi,\psi,hkl)\left\langle \sigma^{s}_{ij} \right\rangle \quad (3)$$

3. Results and discussion

3.1. Surface topography

Fig. 3 illustrates the surface topography of the sample produced with 67° scan rotation (state-of-the-art) with applied contour in as-built condition and post-processed by CMP. The as-built surface (Fig. 3a,b) exhibits the characteristic roughness of PBF-LB, with randomly distributed peaks and valleys due to adhered powder and solidified melt pools [3]. This results in a measured surface roughness of $Sa = 15.9$ µm and a large distance between peaks and valleys ($S10z = 156$ µm), as detailed in Table 2. Following CMP, a dramatic reduction in surface roughness is observed (Fig. 3c,d). The Sa value decreases to 1.5 µm, indicating a significant smoothing effect. With most of the peaks present in the as-built condition being effectively removed, the surface is flat but still shows some valleys. As described above, the CMP process primarily targets the peaks. After a material removal of approximately 110 µm, that basically aims to remove the adhered powder, a few valleys remain. According to the $S10z$ value after CMP, see Table 2, further material removal of 50 µm would have been required to fully remove the valleys of the 67°-C condition. This peak-selective removal is inherent to the CMP mechanism [20,21]. The chemical compound forms a removable conversion layer primarily on exposed surfaces, which are more accessible to both the reactive chemistry and mechanical rubbing from the media. This results in a self-limiting material removal process that preferentially smooths peaks, consistent with the observed topography in Fig. 3.

The initial scan strategy also plays a role in the resulting surface topography after CMP, as indicated by the roughness measurements, see Table 2, where the Sa value ranged from (0.7–4.4 µm) and the $S10z$ (28.2–98.8 µm) after surface treatment. Using contour showed significant differences for the samples produced with 67° scan rotation, whereas no contour surfaces showed valleys twice as deep (~50 µm vs. ~100 µm for C vs NC) as described by $S10z$. It is seen that 67°-NC had a rougher surface in as-built condition ($Sa = 19.2$ µm) compared to the same orientation with contour applied ($Sa = 15.9$ µm) similar trends were also observed in samples printed with 0° scan rotation. Applying an optimized contour lowers the surface roughness in the as-built condition by smoothing the melt pool boundaries and reducing powder adhesion [4,5].

The orientation of the remaining valleys after CMP is also influenced by the scan rotation (0° vs. 67°), as shown in Fig. 4. Due to the 67° rotation between each processed layer, the surface topography parallel to the build direction is isotropic in as-built condition [25], as seen from the irregular morphology and random valley distribution after CMP processing, see Fig. 4a,b. However, samples produced with a 0° scan

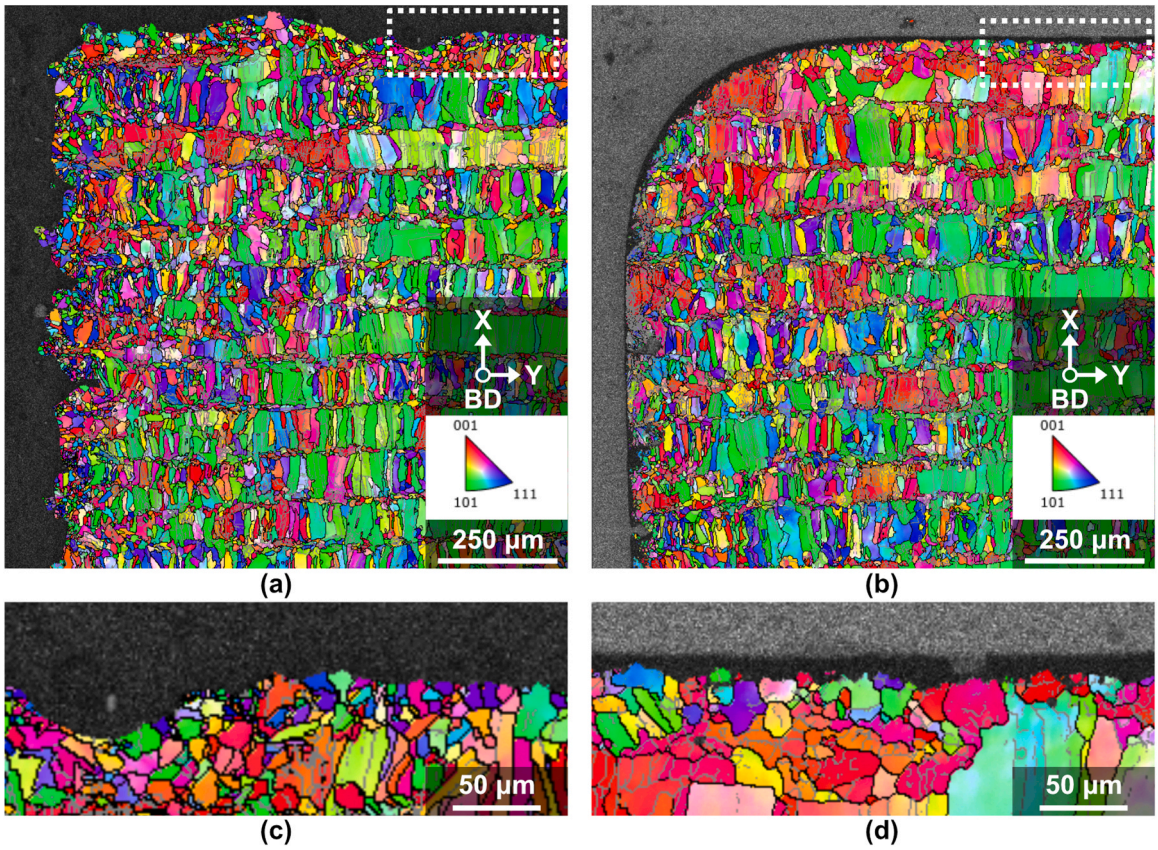

Fig. 6. EBSD maps of XY-cross sections. (a) as-built condition and (b) after CMP where surface smoothening and rounding effect at the corner are visible. Subsets at higher magnifications of the same surfaces, (c) as-built and (d) CMP processed, indicate that the grain size is unaffected by CMP.

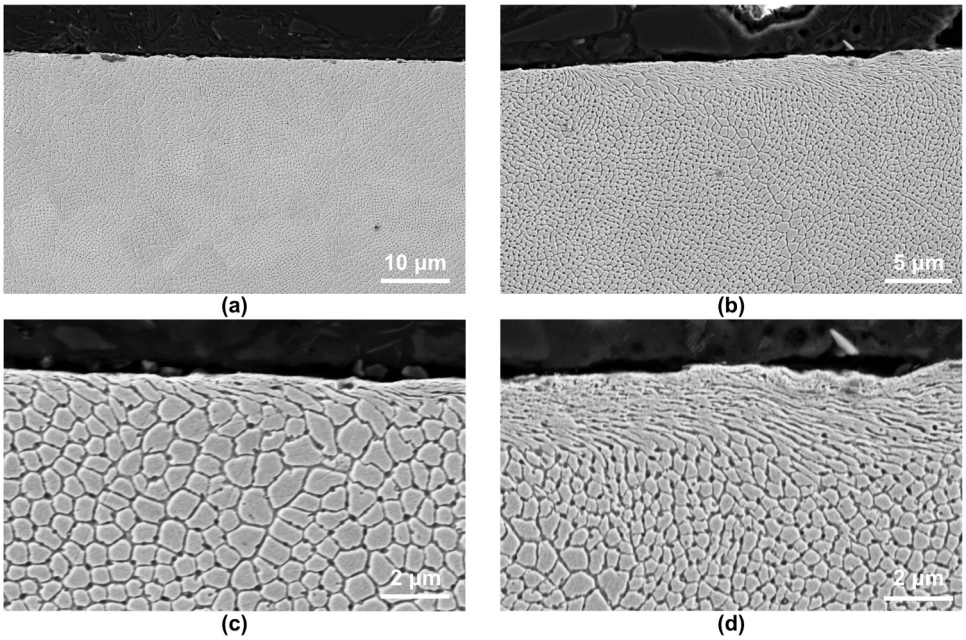

Fig. 7. Etched microstructure of CMP-processed sample. (a) and (c) at the centre of the cube and (b) and (d) at the samples edge.

rotation showed a strong dependence on the number of valleys, their depth, morphology, and orientation with respect to the build direction, see Fig. 4c,d. Only a few randomly distributed valleys are observed for the BD-Y cross-section as opposed to the perpendicular surface BD-X. As insufficient material was removed (Fig. 4d), the powder can be seen in the valleys formed between overlapping melt pools. This indicates that while CMP effectively reduces roughness, the footprint of the initial surface pattern can still be observed unless valleys are successfully removed (Fig. 4c). This observation indicates that the initial surface roughness and pattern, which are themselves influenced by the scan

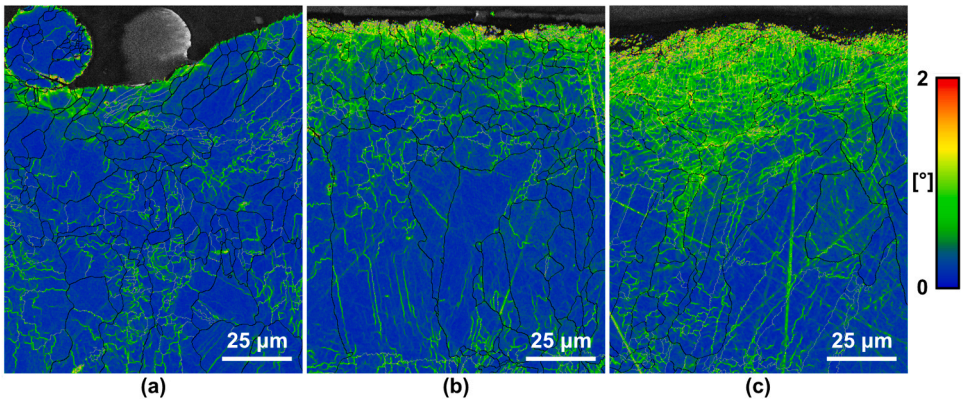

Fig. 8. Kernel Average Misorientation (KAM) maps of the sample surface. (a) as-built condition, (b) face of the cube after CMP, and (c) sample edge after CMP.

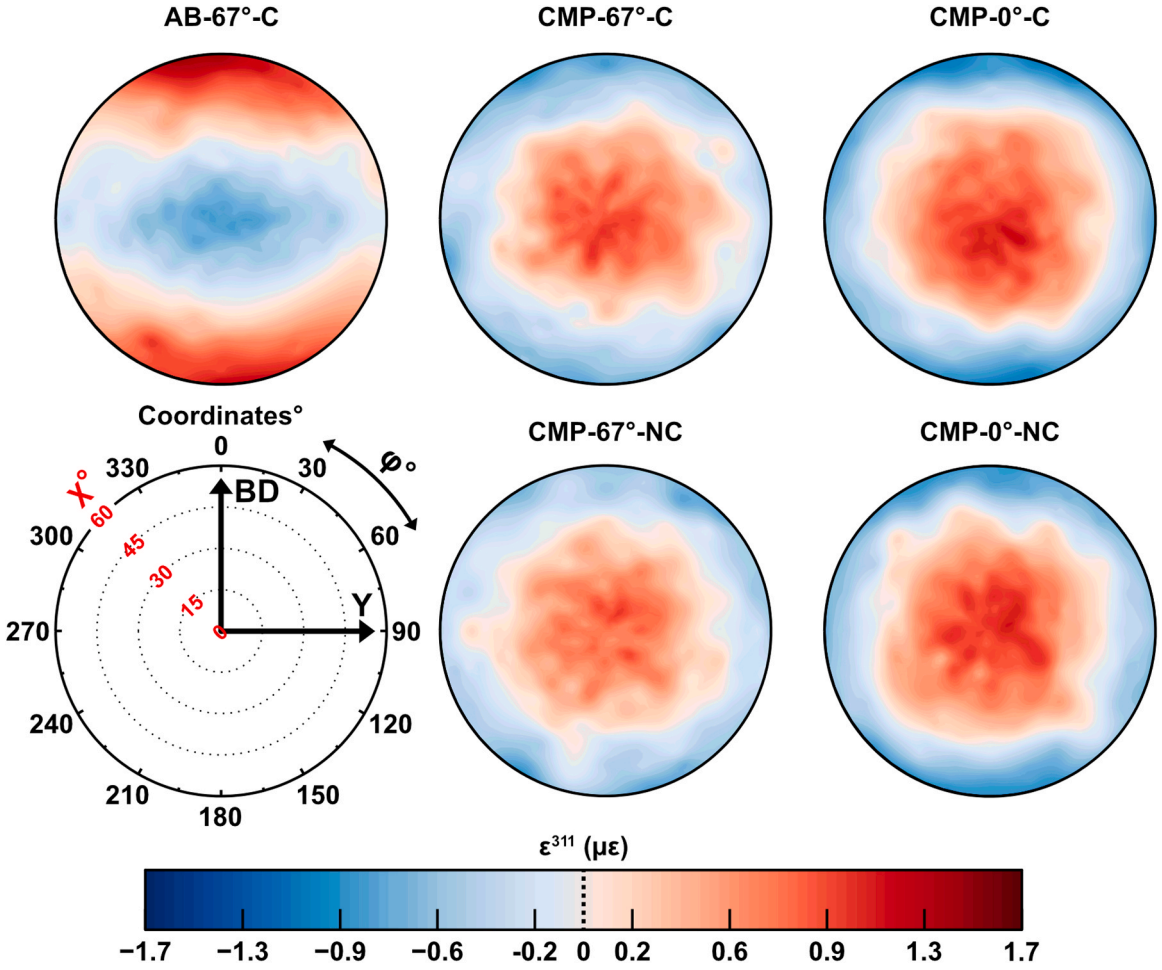

Fig. 9. Strain pole figures from energy-dispersive synchrotron X-ray diffraction measurements, calculated using the 311 reflection. The top left figure shows the as-built condition (AB-67°-C), while the remaining maps represent different CMP-treated surfaces. The bottom left schematic illustrates the φ–χ coordinate system relative to the build direction. The colour scale represents lattice strain $\varepsilon^{3\ 11}$ (με).

strategy, determine the required material removal during CMP to reach isotropic surface topography. To fully optimize the CMP process when treating samples with different as-built surface topography due to, e.g., increased layer thickness, the effectiveness of contour scan, the difference in processing parameters, overhangs, etc., the largest *S10z* value could act as a guidance for required material removal. For example, in the case of 67°-NC samples, *S10z* of ~189.7 µm clearly shows that in this case material removal of ~110 µm was not enough to get to the targeted smooth surface. Knowledge of these relationships is crucial for tailoring the CMP process to achieve the desired surface finish and, ultimately, the desired mechanical properties.

3.2. Microstructure after CMP

To investigate the microstructural impact on CMP treated surfaces and the depth of surface/sub surface features, samples were sectioned and analysed in the XY-plane (perpendicular to build direction).

Fig. 5 illustrates etched cross-sections in the as-built condition and

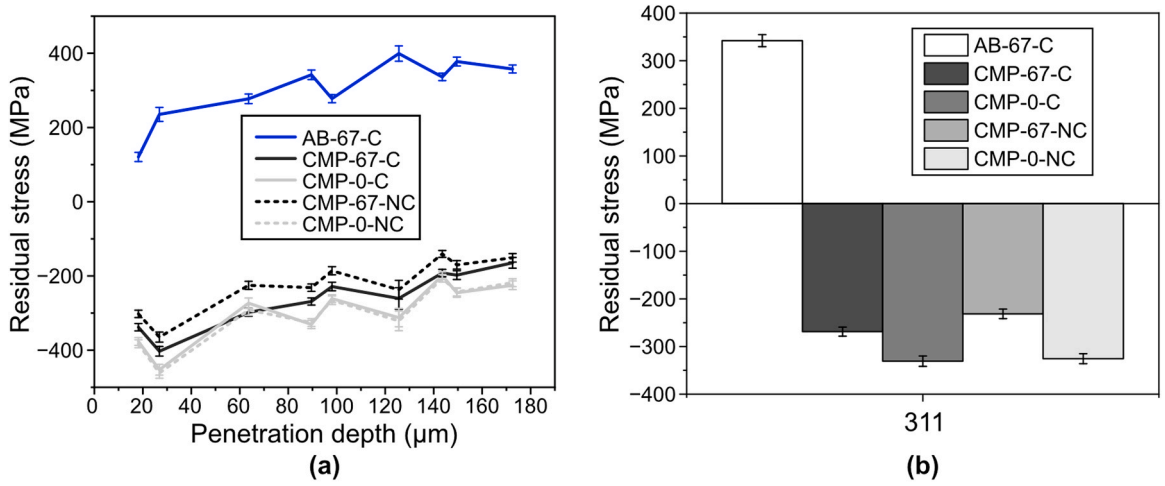

Fig. 10. Deviatoric residual stress obtained by SXRD. (a) depth profile along the building direction and (b) residual stress for 311 reflections with error bars of 2STDEV.

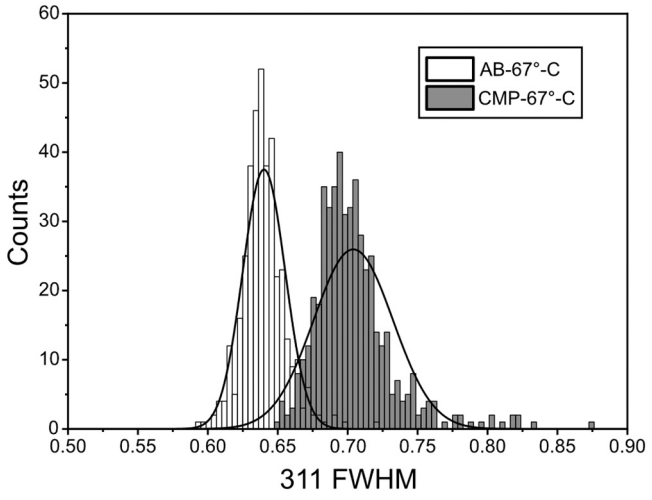

Fig. 11. Full width at half maximum (FWHM) distributions for the 311 reflection in as-built (AB-67°-C) and CMP-processed (CMP-67°-C) samples. The Histograms represent counts of individual measurements obtained via energy-dispersive synchrotron X-ray diffraction and curves are overlaid to visualize the FWHM distribution.

after CMP for 0° scan rotation without contour. The surface features are presented from different perspectives with reference to the scan vectors and solidification direction of the melt pools. The as-built condition (Fig. 5a,c) exhibits irregular features, including adhered powder and primary roughness/waviness from melt pool solidification. Notably, the surface perpendicular to the melt tracks (perpendicular to the scanning vector) (Fig. 5a) has only a small amount of powder and slight waviness with no visible subsurface defects. It is seen that CMP effectively removes these features, resulting in a flat surface (Fig. 5b). However, the surface parallel to the scan vectors (Fig. 5c) shows valleys in the order of 130 μm and some valleys have powder trapped inside them between the overlapping melt pools. This is seen from another perspective on the outer surface in (Fig. 4d). Observations of the same condition after CMP, see Fig. 5d, show that deep valleys of up to 90 μm can be found while the outer surface is planarized. Some valleys are opened by removing the peaks on the as-build surface and some are closed. Despite this clear smoothing, no significant microstructural changes often seen for abrasive processes such as shot peening [15] (ex. grain refinement) are observed at this magnification.

As seen from the EBSD maps in Fig. 6, CMP does not change the microstructure or grain size near the edges. Visually, a rounding of the edges can be clearly seen on the samples, see Fig. 6b. The EBSD maps of the surface at higher magnification (Fig. 6c,d) show that no grains are preferentially attacked, indicating no impact of the microstructure on material removal. The black (unindexed) area at the surface in Fig. 6d suggests the absence of EBSD hits due to a thin, highly-deformed surface layer.

Observation of etched microstructure at higher magnification, see Fig. 7, shows that cells at the surface got deformed. On the face of the cubes, this deformation reaches about 1–2 μm into the material. At the corner of the cube, the deformation is more pronounced, reaching up to 3–5 μm in depth. To further investigate the deformation induced by CMP, high-magnification KAM maps with a step size of 200 nm and a maximum misorientation of 2° were acquired, see Fig. 8. An increase in misorientation from the as-built condition (Fig. 8a) to the surfaces exposed to CMP (Fig. 8b,c), was observed. This increase in misorientation suggests that CMP introduces plastic deformation close to the surface. Increase in misorientation was more prominent at the sample corner (Fig. 8c), compared to the face of the cube, see Fig. 8b. This correlates well with the observed larger area being affected in Fig. 7b.

3.3. Influence of CMP on residual stress

Fig. 9 presents the strain pole figures obtained by ED-SXRD at the P61A beamline. Since ED-SXRD measurements were performed with around 500 acquisitions mapping the sample surfaces around χ and φ, see Fig. 9, the information about stress anisotropy and principal directions can be extracted. The strain pole figures in Fig. 9 show that the maximum principal direction aligns with the building direction, as typically observed in AM parts [37]. However, after CMP, the compressive strains are isotropic around the pole in all φ directions. Hence, CMP not only generates compressive residual stresses at the subsurface but also removes the stress anisotropy.

Fig. 10 presents residual stresses measured along the building direction. Energy dispersive diffraction allows to obtain residual stress as a function of the information depth from the surface, see Fig. 10a. Typically, for as-built conditions, the subsurface stress reaches its maximum around 100–200 μm but having lower values closer to the surface due to high surface roughness effects [38]. After CMP, the stresses become compressive with about –400 MPa at the surface, and the stress increases as a function of depth. Regardless of the initial manufacturing parameter, the stresses remain compressive over the whole range of the measurements (up to 180 μm). It is, therefore, unclear until what depth

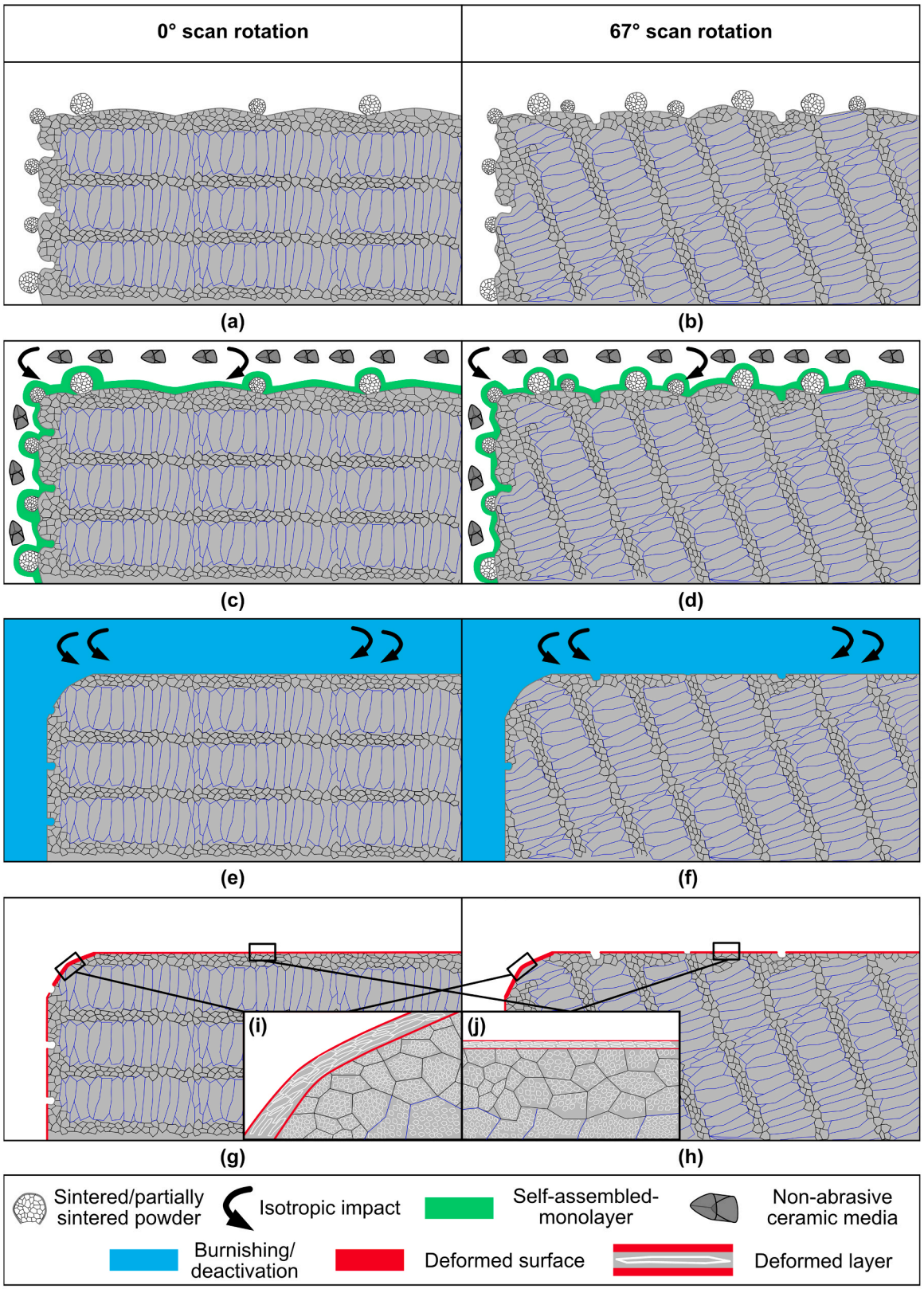

Fig. 12. Microstructural impact on material removal by CMP and process mechanisms. Schematic illustration of the CMP cycle for PBF-LB 316 L stainless steel with 0° (left panels) and 67° (right panels) scan rotation, shown on cross-sections perpendicular to the build direction. (a and b) as-built surfaces, (c and d) chemical activation and vibratory finishing, (e and f) burnishing step, (g and h) final deformed surfaces with remaining surface porosity, and (i and j) thickness of the deformation layer.

in the sample the residual stresses remain compressive. According to stress balance theory, the total stress within the sample should equal zero, suggesting a stress redistribution inside the sample after CMP. This is, however, a topic for further investigations, including stress mapping in the bulk of the material.

For easier comparison, the residual stresses along the build direction for the 311 reflection, corresponding to 90 μm depth, are shown in Fig. 10b. The as-built condition shows a tensile stress of approximately 340 MPa. Notably, the CMP post-treatment induces a compressive stress state of approximately −260 MPa for the sample produced with 67° scan rotation using a contour, see Fig. 10b. This means a 180 % stress reduction at the surface. It is also seen that the scan rotation had an impact on the residual stress distribution since the samples produced with 0° scan rotation show larger compressive stresses of −330 MPa after CMP. In fact, previous work showed that 0° scan rotation generates high anisotropic stress distribution as the solidification always occurs in the same direction [39]. Further, by increasing the scan rotation angle between layers, the stress was more uniform and evenly distributed, thus, explaining the measured differences. Notably, the impact of the contour was minimal on residual stress.

The full width half maximum (FWHM) of the diffraction peaks can be used as a qualitative measure of the plastic deformation/dislocation density. Fig. 11 shows the FWHM distribution of the diffraction peaks (from all acquisitions) measured at the surface of as-built and CMP samples. Much broader peaks for the CMP condition confirm higher plastic deformation at the surface of these samples, in agreement with the KAM maps (Fig. 8).

3.4. Mechanisms and microstructure development during CMP

The combined results of surface topography, microstructure, and residual stress can be explained through the chemical mechanical cycle of CMP, as illustrated in Fig. 12. The as-built surfaces (Fig. 12a,b) contain adhered powder and melt pool waviness, with valley depth and location governed by the scan rotation. Samples built with 0° rotation generally exhibited deeper, directionally aligned valleys, while 67° rotation produced more isotropic features. During the chemical activation step (Fig. 12c,d), a thin brittle conversion layer forms preferentially on surface peaks. This enables peak-selective removal when rubbed by the vibratory media, explaining why CMP effectively removes powder and surface peaks but leaves some deep valleys depending on the initial printing parameters.

The subsequent burnishing step (Fig. 12e,f) deactivates and removes the conversion layer and enhances surface smoothness. EBSD and KAM analysis show that CMP does not alter the bulk grain structure but produces a plastically deformed surface layer (Fig. 12i,j). The deformation depth is limited to 1–5 μm and is more pronounced at edges where media contact is highest. The observed misorientation and unindexed EBSD regions confirm that removal occurs through mechanical removal of the weakened conversion layer, since purely chemical dissolution would not produce localized plasticity.

In the final CMP surface (Fig. 12 g,h), the combined chemical mechanical process results in a smoother surface with some valleys remaining and the transformation of tensile into compressive residual stresses. The smoothing of surface peaks reduces local stress concentrations, while the isotropic vibratory action induces a uniform plastic deformation layer that produces an isotropic compressive strain state. Altogether, CMP operates as a hybrid process in which chemical oxidation creates a removable surface film, mechanical rubbing strips the film and surface peaks, and burnishing removes residual oxide. This cycle explains the observed reduction in roughness, the presence of a thin plastically deformed layer, and the redistribution of surface stresses.

4. Conclusions

The detailed study of the surface and subsurface effects of CMP on PBF-LB 316 L stainless steel with the aim to enhance the performance of inherently rough and complex surfaces produced by PBF-LB is presented. The impact of scan strategy and resulting surface morphology on material removal behaviour, microstructure, and residual stress is shown. While CMP has previously shown promising results in roughness reduction, its mechanistic interaction with anisotropic as-built features and its capacity to modify the surface stress state have remained insufficiently understood. Based on the findings the following conclusions and recommendations are provided:

- The CMP enables controlled surface material removal by selectively removing surface peaks, providing topographic uniformity without altering the surface microstructure. The CMP process reduced the areal surface roughness (*Sa*) by approximately 90 %, achieving values as low as 0.7 μm while preserving the underlying grain structure.
- The initial scan strategy and resulting surface morphology were found to govern the required material removal depth for complete planarization. Samples built with a 0° scan rotation or without contour parameters exhibited deeper surface valleys ($S10z > 100$ μm), requiring material removal exceeding 110 μm to fully eliminate roughness features.
- CMP further demonstrated its effectiveness as a non-abrasive alternative to deformation-based surface treatments by inducing compressive residual stresses through localized surface plastic deformation. Residual stress analysis revealed a transition from tensile stresses of + 340 MPa in the as-built condition to compressive stresses approaching −400 MPa after CMP, with minimal changes to the microstructure.
- The initial microstructure and component geometry influenced the local CMP response, specifically at part edges and corners, where increased media contact resulted in increased plastic deformation. This was confirmed through EBSD and KAM mapping, which revealed enhanced misorientation.
- Lastly, CMP was found to homogenize the surface strain distribution, converting anisotropic strain into isotropic. Strain pole figures derived from synchrotron X-ray diffraction showed that directional strain in the as-built 67° scan condition was eliminated by CMP, resulting in a uniform compressive strain across all directions.

CRediT authorship contribution statement

Rasmus Gunnerek: Writing – original draft, Visualization, Investigation, Conceptualization. **Gowtham Soundarapandiyan:** Writing – review & editing, Visualization, Investigation. **Eduard Hryha:** Writing – review & editing, Supervision, Funding acquisition, Conceptualization. **Agustin Diaz:** Writing – review & editing. **Uta Klement:** Writing – review & editing, Supervision, Conceptualization. **Giovanni Bruno:** Writing – review & editing. **Joshua Boykin:** Writing – review & editing. **Tatiana Mishurova:** Writing – review & editing, Visualization, Investigation. **Jakob Schröder:** Writing – review & editing, Visualization, Investigation.

Funding

This work was performed in the frame of the ProThin project [Dnr: 2021–01273] and the Centre for Additive Manufacture - Metal (CAM^2), both supported by the Swedish Agency for Innovation Systems Vinnova.

Declaration of Competing interest

The authors declare that they have no known competing financial interests or personal relationships that could have appeared to influence

the work reported in this paper.

Acknowledgements

We acknowledge DESY (Hamburg, Germany), a member of the Helmholtz Association HGF, for the provision of beamtime (proposal No. 20240357). In this context, we thank Dr. Guilherme Abreu Faria and Dr. Marc-André Nielsen for assistance in operating the white beam engineering materials beamline P61A.

Data availability

Data will be available upon request.

References

[1] Hovig, E.W., Azar, A.S., Sunding, M.F., Andreassen, E., Sørby, K., 2019. High cycle fatigue life estimation of materials processed by laser powder bed fusion. Fatigue Fract. Eng. Mater. Struct. 42, 1454–1466. https://doi.org/10.1111/ffe.12982.

[2] Shrestha, R., Simsiriwong, J., Shamsaei, N., 2019. Fatigue behavior of additive manufactured 316L stainless steel parts: effects of layer orientation and surface roughness. Addit. Manuf. 28, 23–38. https://doi.org/10.1016/j.addma.2019.04.011.

[3] Snyder, J.C., Thole, K.A., 2020. Understanding laser powder bed fusion surface roughness. J. Manuf. Sci. Eng. 142. https://doi.org/10.1115/1.4046504.

[4] Artzt, K., Mishurova, T., Bauer, P.P., Gussone, J., Barriobero-Vila, P., Evsevleev, S., Bruno, G., Requena, G., Haubrich, J., 2020. Pandora's box-influence of contour parameters on roughness and subsurface residual stresses in laser powder bed fusion of Ti-6Al-4V. Materials 13, 1–24. https://doi.org/10.3390/ma13153348.

[5] Reiber, T., Rüdesheim, J., Weigold, M., Abele, E., Musekamp, J., Oechsner, M., 2021. Influence of contour scans on surface roughness and pore formation using Scalmalloy® manufactured by laser powder bed fusion (PBF-LB). Materwiss Werksttech 52, 468–481. https://doi.org/10.1002/mawe.202000287.

[6] Kruth, J.P., Deckers, J., Yasa, E., Wauthlé, R., 2012. Assessing and comparing influencing factors of residual stresses in selective laser melting using a novel analysis method. Proc. Inst. Mech. Eng. B J. Eng. Manuf. 226, 980–991. https://doi.org/10.1177/0954405412437085.

[7] Sandmann, P., Keller, S., Kashaev, N., Ghouse, S., Hooper, P.A., Klusemann, B., Davies, C.M., 2022. Influence of laser shock peening on the residual stresses in additively manufactured 316L by laser powder bed fusion: a combined experimental–numerical study. Addit. Manuf. 60, 103204. https://doi.org/10.1016/J.ADDMA.2022.103204.

[8] Ardi, D.T., Guowei, L., Maharjan, N., Mutiargo, B., Leng, S.H., Srinivasan, R., 2020. Effects of post-processing route on fatigue performance of laser powder bed fusion inconel 718. Addit. Manuf. 36. https://doi.org/10.1016/j.addma.2020.101442.

[9] Strauß, L., Pang, G.A., Löwisch, G., 2024. Fatigue life prediction of additively manufactured AlSi10Mg based on surface roughness and residual stress. Fatigue Fract. Eng. Mater. Struct. 47, 4465–4477. https://doi.org/10.1111/ffe.14441.

[10] Lee, S., Pegues, J., Shamsaei, N., 2019. Fatigue behavior of additive manufactured 304L stainless steel including surface roughness effects. Solid Freeform Fabrication 2019: Proceedings of the 30th Annual International Solid Freeform Fabrication Symposium - An Additive Manufacturing Conference, SFF, pp. 376–387.

[11] Snyder, J.C., Stimpson, C.K., Thole, K.A., Mongillo, D.J., 2015. Build direction effects on microchannel tolerance and surface roughness. J. Mech. Des. 137. https://doi.org/10.1115/1.4031071.

[12] Zeidler, H., Böttger-Hiller, F., Krinke, S., Parenti, P., Annoni, M., 2019. Surface finish of additively manufactured parts using plasma electrolytic polishing. European Society for Precision Engineering and Nanotechnology, Conference Proceedings - 19th International Conference and Exhibition, EUSPEN 2019, 2019, pp. 228–229.

[13] Hashmi, A.W., Mali, H.S., Meena, A., Puerta, A.P.V., Kunkel, M.E., 2022. Surface characteristics improvement methods for metal additively manufactured parts: a review. Adv. Mater. Process. Technol. 8, 4524–4563. https://doi.org/10.1080/2374068X.2022.2077535.

[14] Cao, S., Zhang, H., Hu, J., Li, C., Li, B., 2024. Fatigue life prediction model for shot-peened laser powder bed fused 304L steel considering residual stress relaxation and defect distribution. Eng. Fail Anal. 162. https://doi.org/10.1016/j.engfailanal.2024.108423.

[15] Gundgire, T., Santa-aho, S., Rautio, T., Järvenpää, A., Vippola, M., 2024. Synergistic effects of heat treatments and severe shot peening on residual stresses and microstructure in 316L stainless steel produced by laser powder bed fusion. J. Mater. Process Technol. 323. https://doi.org/10.1016/j.jmatprotec.2023.118229.

[16] Maleki, E., Bagherifard, S., Razavi, N., Riccio, M., Bandini, M., du Plessis, A., Berto, F., Guagliano, M., 2022. Fatigue behaviour of notched laser powder bed fusion AlSi10Mg after thermal and mechanical surface post-processing. Mater. Sci. Eng. A 829. https://doi.org/10.1016/j.msea.2021.142145.

[17] Tyagi, P., Goulet, T., Riso, C., Garcia-Moreno, F., 2019. Reducing surface roughness by chemical polishing of additively manufactured 3D printed 316 stainless steel components. Int. J. Adv. Manuf. Technol. 100, 2895–2900. https://doi.org/10.1007/s00170-018-2890-0.

[18] Zhang, J., Wang, H., 2022. Magnetically driven internal finishing of AISI 316L stainless steel tubes generated by laser powder bed fusion. J. Manuf. Process 76, 155–166. https://doi.org/10.1016/j.jmapro.2022.02.009.

[19] Demeneghi, G., Gradl, P., Diaz, A., Hazeli, K., 2024. Effect of surface finish and temperature on low cycle fatigue behavior of GRCop-42. Fatigue Fract. Eng. Mater. Struct. 840–856. https://doi.org/10.1111/ffe.14526.

[20] Prochaska, S., Hildreth, O., 2022. Microstructural and corrosion effects of HIP and chemically accelerated surface finishing on laser powder bed fusion alloy 625. Int. J. Adv. Manuf. Technol. 121, 3759–3769. https://doi.org/10.1007/s00170-022-09579-1.

[21] Witkin, D.B., Patel, D.N., Helvajian, H., Steffeney, L., Diaz, A., 2019. Surface treatment of Powder-Bed fusion additive manufactured metals for improved fatigue life. J. Mater. Eng. Perform. 28, 681–692. https://doi.org/10.1007/s11665-018-3732-9.

[22] Diaz, A., McFadden, P., Garcia-Avila, M., Scovill, J., 2022. Surface texture optimization of metal additive manufactured components through Chemical-Mechanical polishing to improve mechanical and corrosion resistance performance. World PM 2022 Congr. Proc. 15–18.

[23] Prochaska, S., Hildreth, O., 2022. Effect of chemically accelerated vibratory finishing on the corrosion behavior of laser powder bed fusion 316L stainless steel. J. Mater. Process Technol. 305, 117596. https://doi.org/10.1016/j.jmatprotec.2022.117596.

[24] Leicht, A., Yu, C.H., Luzin, V., Klement, U., Hryha, E., 2020. Effect of scan rotation on the microstructure development and mechanical properties of 316L parts produced by laser powder bed fusion. Mater. Charact. 163, 110309. https://doi.org/10.1016/j.matchar.2020.110309.

[25] Gunnerek, R., Soundarapandiyan, G., Christoph, M., Hryha, E., Klement, U., 2024. Transactions of the IMF the international journal of surface engineering and coatings influence of microstructure and surface topography on material removal by the hirtisation ® process. Trans. IMF 0, 1–8 https://doi.org/10.1080/00202967.2024.2411903.

[26] I.S.F. Process for Metal Superfinishing- REM Surface Engineering, (n.d.). https://www.remchem.com/technology/processes/isf-process/ (accessed March 20, 2025).

[27] Cabanettes, F., Joubert, A., Chardon, G., Dumas, V., Rech, J., Grosjean, C., Dimkovski, Z., 2018. Topography of as built surfaces generated in metal additive manufacturing: a multi scale analysis from form to roughness. Precis Eng. 52, 249–265. https://doi.org/10.1016/j.precisioneng.2018.01.002.

[28] SIS (Swedish Standards Institute), Svensk Standard, Ss 812310:2014 (2018) 24. www.sis.se.

[29] Farla, R., Bhat, S., Sonntag, S., Chanyshev, A., Ma, S., Ishii, T., Liu, Z., Néri, A., Nishiyama, N., Faria, G.A., Wroblewski, T., Schulte-Schrepping, H., Drube, W., Seeck, O., Katsura, T., 2022. Extreme conditions research using the large-volume press at the P61B endstation, PETRA III. J. Synchrotron Radiat. 29, 409–423. https://doi.org/10.1107/S1600577522001047.

[30] Giessen, B.C., Gordon, G.E., 1979. X-ray diffraction: new High-Speed technique based on X-ray spectrography. Science 159 (1968), 973–975. https://doi.org/10.1126/SCIENCE.159.3818.973.B.

[31] Genzel, C., 1994. Formalism for the evaluation of strongly non-linear surface stress fields by X-ray diffraction performed in the scattering vector mode. Phys. Status Solidi (a) 146 629–637. https://doi.org/10.1002/pssa.2211460208.

[32] P61A Toolkit Documentation — P61A Toolkit documentation, (n.d.). https://hereon-gems.github.io/P61AToolkit/ (accessed March 12, 2025).

[33] Ortner, B., 2011. The matrix method for data evaluation and its advantages in comparison to the Sin2ε and similar methods. Mater. Sci. Forum 681, 7–12. https://doi.org/10.4028/www.scientific.net/MSF.681.7.

[34] Welzel, U., Mittemeijer, E.J., 2003. Diffraction stress analysis of macroscopically elastically anisotropic specimens: on the concepts of diffraction elastic constants and stress factors. J. Appl. Phys. 93, 9001–9011. https://doi.org/10.1063/1.1569662.

[35] Predicted single-crystal elastic constants of stainless-steel 316, (n.d.). https://inis.iaea.org/records/0f283-hgb43 (accessed March 12, 2025).

[36] Gnäupel-Herold, T., 2012. ISODEC: software for calculating diffraction elastic constants. J. Appl. Crystallogr 45, 573–574. https://doi.org/10.1107/S0021889812014252.

[37] Schröder, J., Evans, A., Luzin, V., Abreu Faria, G., Degener, S., Polatidis, E., Čapek, J., Kromm, A., Dovzhenko, G., Bruno, G., Keckes, J., 2023. Texture-based residual stress analysis of laser powder bed fused inconel 718 parts. J. Appl. Crystallogr 56, 1076–1090. https://doi.org/10.1107/S1600576723004855.

[38] Mishurova, T., Artzt, K., Haubrich, J., Requena, G., Bruno, G., 2019. Exploring the correlation between subsurface residual stresses and manufacturing parameters in laser powder bed fused ti-6al-4v. Metals 9. https://doi.org/10.3390/met9020261.

[39] Ezura, A., Abe, S., Furumoto, T., Sasaki, T., Sakamoto, J., 2023. Study on laser scan strategy for correcting anisotropic residual stress distribution and reducing warpage in structures fabricated by PBF-LB/M. Int. J. Autom. Technol. 17, 369–377. https://doi.org/10.20965/ijat.2023.p0369.